AIMS Mathematics, 11(4): 10566–10588.
DOI: 10.3934/math.2026435
Received: 12 February 2026
Revised: 01 April 2026
Accepted: 14 April 2026
Published: 17 April 2026

https://www.aimspress.com/journal/Math

Research article

A new efficient symbolic computation fusion neural network method: Solving exact solutions of (3+1)-dimensional nonlinear partial differential equations

Yu Gao[1], **Jingwen Huang**[1], **Baoying Du**[1] **and Jianglong Shen**[1,2,*]

[1] School of Mathematics and Physics, Yibin University, College Street, Yibin 644000, Sichuan, China

[2] Key Laboratory of Computational Physics of Sichuan Province, Yibin University, College Street, Yibin 644000, Sichuan, China

* **Correspondence:** Email: jlshen@yibinu.edu.cn.

Abstract: This study proposed a novel symbolic computing algorithm based on neural networks for solving the (3+1)–dimensional Jimbo-Miwa equation. By constructing a direct neural network model and integrating neural networks with symbolic computing, activation functions were assigned to the neurons in the hidden layer of the neural network. After deriving the trial function, symbolic computing using Maple was employed to obtain the exact analytical solution of the equation. Our innovative method effectively avoids the reliance on large datasets and low computational efficiency of traditional methods. Based on this improved method, we have constructed single-hidden-layer and double-hidden-layer neural network models to solve the equation's exact solutions, and successfully obtained breather solutions, shock wave solutions, and lump solutions. The successful solution of the equation in this study fully demonstrates the efficiency of the constructed framework and indicates its promising application prospects in other important nonlinear partial differential equation fields.

Keywords: (3+1)–dimensional Jimbo–Miwa equation; symbolic–neural integration; exact solution; neural network; nonlinear partial differential equation
Mathematics Subject Classification: 35A25, 35Q51

1. Introduction

Nonlinear partial differential equations (NLPDEs) provide indispensable mathematical frameworks for modeling complex phenomena across diverse scientific and engineering domains, including biology [1], quantum mechanics [2], financial mathematics [3], fluid mechanics [4], optics [5, 6], and plasma physics [7]. Their capacity to accurately capture intricate system behaviors

underpins critical applications, exemplified by the Navier-Stokes equations in aerospace engineering [8] and meteorological forecasting [9].

Among integrable NLPDEs of significant theoretical and applied interest is the Jimbo–Miwa equation, originally introduced by Jimbo and Miwa [10]. This equation finds broad relevance within mathematical and theoretical physics. Its (3+1)–dimensional variant, defined across three spatial dimensions and one temporal dimension, offers a powerful model for investigating complex wave propagation and interaction dynamics in higher dimensions. The equation reads:

$$u_{xxxy} + 3u_y u_{xx} + 3u_x u_{xy} + 2u_{yt} - 3u_{xz} = 0, \tag{1.1}$$

where u(x, y, z, t) represents a potential function, often interpreted physically as the amplitude or field evolution potential of a high–dimensional nonlinear wave. The structure of Eq (1.1) reveals key dynamical components: The terms $3u_y u_{xx} + 3u_x u_{xy}$ constitute the nonlinearity and driving waveform distortion through self-modulation. The fourth-order mixed derivative u_{xxxy} acts as a higher-order dispersion term, counteracting nonlinear effects to enable stable structures like solitons. The cross-derivative terms $2u_{yt} - 3u_{xz}$ introduce multidimensional coupling, constraining the wave evolution across space-time and enabling the existence of localized lumps, oblique waves, and genuine (3+1)–dimensional solitons. Consequently, the (3+1)–dimensional Jimbo–Miwa equation serves as a cornerstone model for exploring intricate three–dimensional nonlinear wave phenomena, particularly in plasma physics [11–13].

The quest for exact solutions to the Jimbo–Miwa equation solitons [14, 15], breathers [16, 17], rogue waves [18, 19] and lumps and their interactions [20] remains a vibrant area of research. Such solutions provide profound insights into nonlinear wave dynamics and underpin theoretical advances in NLPDEs, while also offering mathematical foundations for understanding complex physical systems [21]. Numerous analytical techniques have been deployed to tackle this equation. These include: Hirota's bilinear method, used to systematically derive lump and lump-like solutions via Bell polynomials [22]; the (G'/G)-expansion method and its variants, yielding traveling wave solutions expressed through hyperbolic, trigonometric, and rational functions [23, 24]; Bell polynomial schemes combined with Bäcklund transformations, Lax pairs, and the three-wave method for constructing bilinear forms and periodic waves [25]; and test function approaches aided by symbolic computation for finding solitary wave solutions [26, 27].

Nevertheless, significant challenges persist. The efficacy of these methods often depends heavily on the specific equation structure or the anticipated solution form (e.g., traveling vs. non-traveling waves, solutions with arbitrary functions) [28]. Crucially, transforming a given NLPDE into the Hirota bilinear form—a powerful route to exact solutions—is not always feasible, limiting applicability. Even when successful, the resulting bilinear system for high–dimensional or complex NLPDEs can involve intricate symbolic computations, especially when constructing solutions with numerous parameters (e.g., ensuring analyticity for a 15-parameter lump solution [29]). This computational burden underscores the need for more robust and efficient methods for deriving exact solutions.

Neural networks have evolved from domain-specific models into a foundational infrastructure supporting cross-disciplinary research. This progression is evident across several dimensions: processing of complex multimodal data, realization of intelligent control and optimization, and development of efficient distributed computing frameworks. In multimodal learning, transformer-based architectures with cross-attention mechanisms have markedly improved performance on tasks such as load forecasting [30]. In systems control and robotics, neural networks have driven advances in controllability analysis of fractional-order impulsive switched systems [31], fuzzy actor-critic learning control [32], hovering control of unmanned aerial vehicles [33], and motion planning for robots under energy constraints [34]. For large-scale artificial intelligence (AI) infrastructure, evaluation frameworks [35], energy-efficiency optimization [36], and resource pricing mechanisms [37] have been established, thereby ensuring sustainable development. In distributed computing paradigms, federated learning frameworks have been effectively applied to Synthetic Aperture Radar (SAR) image generation [38] and target recognition [39]. Further breakthroughs have been achieved in visual and spatiotemporal sequence tasks, including video deblurring [40], event-based camera representation [41], and traffic conflict identification [42]. Training efficiency of deep networks has been enhanced from an optimization perspective through gradient-system-focused methods [43]. Collectively, these developments demonstrate the profound expansion of neural networks as a core tool across theoretical foundations, methodological innovations, and application breadth.

Recent advances in neural networks (NNs) offer promising new paradigms for solving NLPDEs. The theoretical foundation, established by the universal approximation theorem [44], guarantees that NNs can approximate complex continuous functions. Physics-informed neural networks (PINNs) [45] embed PDE residuals directly into the loss function, enabling solution discovery even with sparse data. Building on this, the bilinear neural network method (BNNM) [46] represents a significant innovation. The BNNM synergizes the expressive power of neural networks with the analytical structure of Hirota's bilinear form, efficiently generating exact analytical solutions—such as solitons, breathers, and rogue waves—critical to fields like optics and fluid mechanics.

Recent extensions and enhancements of the BNNM have further demonstrated its versatility and effectiveness. These include a new neural-symbolic framework integrating symbolic computation for the (2+1)-dimensional Boussinesq equation [47], a bilinear feature-enhanced symbolic computation neural network approach for the (1+1)-dimensional Caudrey–Dodd–Gibbon equation [48], bilinear neural network computations yielding lump interactions and rogue waves in the (2+1)-dimensional Kairat-II-X-type model [49], and investigations of inelastic lump–breather interactions together with periodic wave dynamics in the generalized Calogero–Bogoyavlenskii–Schiff equation [50]. The BNNM has also shown notable success in solving various other NLPDEs, yielding breathers and interacting solitons for the (2+1)D Hirota–Satsuma–Ito equation [51], novel test functions and rogue waves for generalized breaking wave equations [52], periodic solitons for the (3+1)-dimensional Boiti–Leon–Manna–Pempinelli (BLMP) equation [53], lump and bright-dark soliton solutions for the (3+1)-dimensional Geng equation [54], and M-lump and lump-breather solutions for the KP-BBM equation [55].

Although the BNNM is well-established for constructing exact solutions to nonlinear partial differential equations (PDEs), two significant limitations are identified. First, a heavy reliance on the bilinear form of the equations is required. The transformation of a general nonlinear equation into its bilinear counterpart often demands extensive mathematical intuition and experience. Consequently, a high entry barrier is created for researchers in engineering fields. This complexity hinders the direct application of the method to practical engineering problems, where the revelation of nonlinear physical mechanisms is essential. Second, the scale of symbolic computation involved in the BNNM increases dramatically when high-dimensional or multi-parameter equations are encountered. This leads to reduced computational efficiency. The ability of the method to handle a broader range of equation types is therefore restricted. These two constraints limit the further adoption of the BNNM in engineering computations. To address these challenges, a more direct and universal algorithm, the neural network symbolic computation algorithm (NNSCA), is developed in this study. Dependence on bilinear forms is eliminated. The original equations are processed directly. Neural network trial functions with explicit mathematical expressions are constructed. Constraint equations are then automatically derived through symbolic computation. By using this framework, various types of exact solutions are systematically obtained. The requirement for complex mathematical transformations is reduced by this approach. Furthermore, a scalable computational framework for high-dimensional nonlinear problems is provided. Wider applications in engineering sciences are anticipated for this method.

The (3+1)–dimensional Jimbo–Miwa equation is investigated using the NNSCA method. For the first time, the automated discovery of diverse analytical solutions is achieved. These solutions include solitons, lump waves, and periodic waves. Key dynamical features are clearly revealed through three-dimensional surfaces and space-time slices. Furthermore, high-dimensional projections are utilized to illustrate wave localization, periodicity, and complex inter-dimensional coupling mechanisms. The advantages of NNSCA over existing methodologies are significant. Unlike the BNNM, the requirement for complex manual transformations is eliminated. Superior precision is maintained compared to PINNs. Additionally, computational costs are minimized as hardware requirements are substantially reduced. The effectiveness of this framework for high-dimensional nonlinear systems is thoroughly validated.

The remainder of this paper is structured as follows: Section 2 details the foundational principles and procedural steps of the NNSCA for solving NLPDEs. Section 3 demonstrates the method's application to the (3+1)–dimensional Jimbo–Miwa equation using single-hidden-layer neural network models, presenting analytical solutions derived from two distinct coefficient sets alongside visualizations. Section 4 enhances model complexity with a two-hidden-layer architecture, solving the same equation and illustrating results using two further coefficient sets. Finally, Section 5 concludes the study.

2. Principles of the NNSCA

This study mainly uses the NNSCA to solve the analytical solution of the (3+1)–dimensional Jimbo–Miwa equation and visualize its analytical solution. The specific solution structure of the NNSCA is shown in Figure 1.

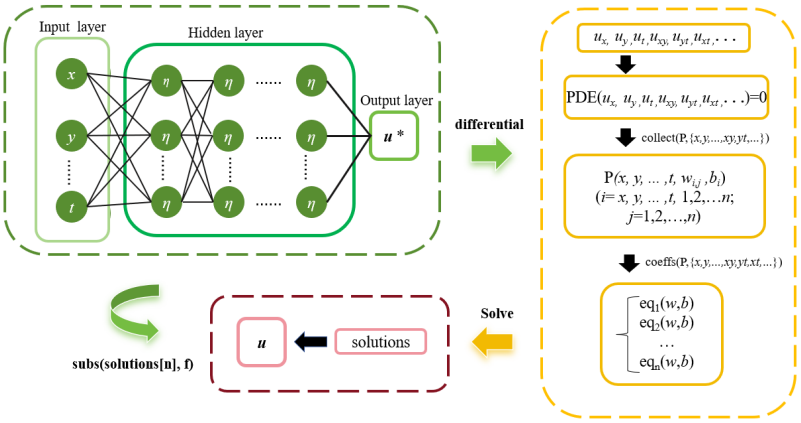

Figure 1. NNSCA method flowchart.

Step 1: Building a high-dimensional neural network architecture. We construct a multi-layer perceptron architecture adapted to (3+1)–spatial-temporal dimensions, with the input layer connected to independent variables $\{x, y, z, t\}$ to capture four-dimensional coupling effects. The hidden layer uses a customized family of activation functions that combine hyperbolic, trigonometric, and exponential functions to adapt to the local and periodic characteristics of high-dimensional waves, breaking through the traditional symbolic method's assumption of solution forms and adaptively exploring the complex solution space containing solitons, lumps, and periodic waves. The output layer directly defines the probe function $f(x, y, z, t)$, leveraging the degrees of freedom of network weights and biases to pre-construct the expression form of high-dimensional solutions.

Step 2: Symbolic derivation of partial derivatives of all orders. Using the Maple symbolic computation engine, we perform a full-order partial derivative expansion of the output u^*, covering all derivative terms involved in the (3+1)–dimensional Jimbo–Miwa equation. We recursively process composite operations using the chain rule to strictly ensure the mathematical rigor of the differential derivation, avoiding numerical differentiation truncation errors, and providing accurate derivative support for subsequent equation substitution.

Step 3: Symbolic mapping of the target PDE. We substitute the partial derivatives of u^* into the (3+1)–dimensional Jimbo–Miwa equation. Through algebraic operations such as rationalization and combining like terms, we gradually eliminate terms directly associated with the unknown solution, transforming it into an equation containing only u^* and its partial derivatives, neural network weights, and biases. This process achieves a dimensionality reduction mapping from partial differential constraints to algebraic constraints, transforming the infinite-dimensional function constraints of the high-dimensional PDE into finite-dimensional algebraic constraints on the network parameters.

Step 4: Construction of the parameter constraint equation system. For the transformed equations, we group terms by spatial-temporal variable powers and neural network parameters, and use the "like-term collection" feature of symbolic computation to extract the coefficient functions for each group of terms. We force all coefficients to zero to ensure the validity of the PDE, generating an algebraic constraint equation system for neural network weights and biases. We compress the parameter space through sparsification processing, constraining the range of free parameters in the neural network to the subspace satisfying the PDE solution.

Step 5: Symbolic solution and constraint screening. We call the Maple symbolic solver to

analyze the constraint system of equations and address the challenge of nonlinear multi-solution: we combine the physical constraints and mathematical constraints of the (3+1)–dimensional Jimbo–Miwa equation to screen for valid solutions, obtain parameter analytical relationships or specific parameter values, and establish a mapping between network parameters and high-dimensional wave physical quantities.

Step 6: Constraint back-substitution and closed-loop verification. We substitute the obtained parameters back into the initial probe function u^* to reconstruct the exact probe function u^* that satisfies the PDE constraints. We conduct symbolic verification by substituting into the (3+1)–dimensional Jimbo–Miwa equation, i.e., we use Maple to recalculate the derivatives and verify the validity of the equation, forming a closed-loop process from neural network pre-exploration to symbolic constraint derivation, parameter solution, and final back-substitution verification, ultimately outputting a (3+1)–dimensional analytical solution that strictly satisfies the equation.

3. Single layer

3.1. Model [4-3-1]-1

To solve the (3+1)–dimensional Jimbo–Miwa equation (1.1), we designed a single-layer neural network model diagram based on the characteristics of the equation, as shown in Figure 2(a). This single-layer neural network model diagram is Model [4-3-1], where the input layer has four neurons, namely, x, y, z, and t, the hidden layer has three neurons $F_1(\xi_1)$, $F_2(\xi_2)$, and $F_3(\xi_3)$, and the output layer is the output probe function $f(x, y, z, t)$.

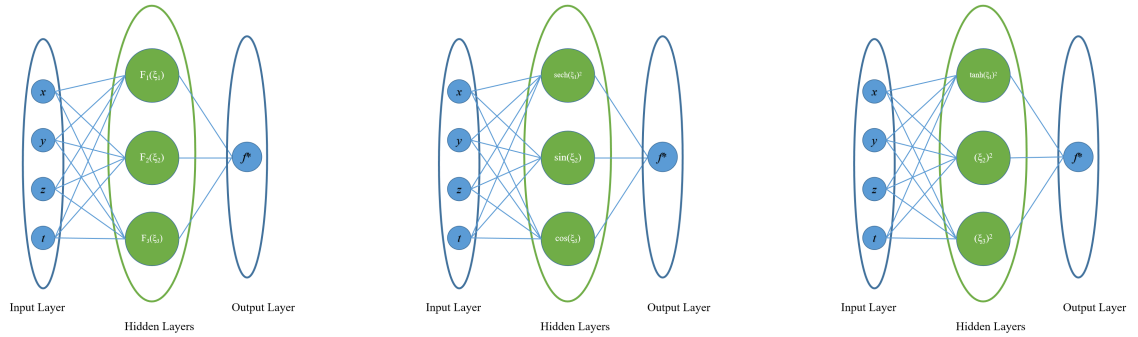

Figure 2. Single-hidden-layer neural network model diagram: (**a**) network structure; (**b**) Model [4-3-1]-1; (**c**) Model [4-3-1]-2.

Now, based on the single-layer neural network model diagram (Figure 2), we construct the activation functions. We set the activation functions $F_1(\xi_1) = \text{sech}^2(\xi_1)$, $F_2(\xi_2) = \sin(\xi_2)$, and $F_3(\xi_3) = \cos(\xi_3)$, resulting in the model shown in Figure 2(b), [4-3-1]-1. By outputting the neural network model, we obtain the test function (3.1):

$$\begin{aligned} u^* = b_4 &+ w_{1,u} \cdot \text{sech}^2\left(t \cdot w_{t,1} + x \cdot w_{x,1} + y \cdot w_{y,1} + z \cdot w_{z,1} + b_2\right) \\ &+ w_{2,u} \cdot \sin\left(t \cdot w_{t,2} + x \cdot w_{x,2} + y \cdot w_{y,2} + z \cdot w_{z,2} + b_3\right) \\ &+ w_{3,u} \cdot \cos\left(t \cdot w_{t,3} + x \cdot w_{x,3} + y \cdot w_{y,3} + z \cdot w_{z,3} + b_5\right). \end{aligned} \tag{3.1}$$

We differentiate the test function (3.1) and substitute it back into (1.1) to obtain a more complex equation. We collect the coefficients of each term to obtain the corresponding underdetermined nonlinear algebraic equation system. We then use Maple to solve this equation system and obtain two sets of coefficient solutions, Case 1 and Case 2, as shown in (3.2) and (3.3), respectively.

$$\textbf{Case 1:}\quad \begin{cases} w_{1,u} = w_{1,u}, & w_{2,u} = w_{2,u}, & w_{3,u} = w_{3,u}, \\ w_{t,1} = \frac{3w_{z,1}(w_{y,1}+w_{z,1})}{2w_{y,1}}, & w_{t,2} = w_{t,2}, & w_{t,3} = \frac{3w_{z,3}(w_{y,3}+w_{z,3})}{2w_{y,3}}, \\ w_{x,1} = 0, & w_{x,2} = 0, & w_{x,3} = 0, \\ w_{y,1} = w_{y,1}, & w_{y,2} = 0, & w_{y,3} = w_{y,3}, \\ w_{z,1} = w_{z,1}, & w_{z,2} = 0, & w_{z,3} = w_{z,3}. \end{cases} \tag{3.2}$$

$$\textbf{Case 2:}\quad \begin{cases} w_{1,u} = w_{1,u}, & w_{2,u} = w_{2,u}, & w_{3,u} = w_{3,u}, \\ w_{t,1} = \frac{3w_{z,1}(w_{y,1}+w_{z,1})}{2w_{y,1}}, & w_{t,2} = \frac{3w_{z,2}(w_{y,2}+w_{z,2})}{2w_{y,2}}, & w_{t,3} = \frac{3w_{z,3}(w_{y,3}+w_{z,3})}{2w_{y,3}}, \\ w_{x,1} = 0, & w_{x,2} = 0, & w_{x,3} = 0, \\ w_{y,1} = w_{y,1}, & w_{y,2} = w_{y,2}, & w_{y,3} = w_{y,3}, \\ w_{z,1} = w_{z,1}, & w_{z,2} = w_{z,2}, & w_{z,3} = w_{z,3}. \end{cases} \tag{3.3}$$

For Case 1, we substitute Eq (3.2) into (3.1). Simplifying the result yields the analytical solution for the (3+1)–dimensional Jimbo–Miwa equation, as shown in Eq (3.4).

$$\begin{aligned} u = b_4 + w_{1,u} \cdot \operatorname{sech}^2\left(\frac{2yw_{y,1}^2 + ((3t+2z)w_{z,1} + 2b_2)\, w_{y,1} + 3tw_{z,1}^2}{2w_{y,1}}\right) \\ + w_{2,u} \cdot \sin\left(tw_{t,2} + b_3\right) + w_{3,u} \cdot \cos\left(\frac{3tw_{z,3}(w_{y,3} + w_{z,3})}{2w_{y,3}} + yw_{y,3} + zw_{z,3} + b_5\right). \end{aligned} \tag{3.4}$$

To confirm the accuracy of the solution in Eq (3.4), we insert the analytical solution into the left-hand side of the (3+1)–dimensional Jimbo–Miwa equation (1.1) and employ Maple software to streamline the outcome. The process reveals that the left-hand side of Eq (1.1) consistently equals zero. This demonstrates that the analytical solution (3.4) is both precise and error-free, while also underscoring the superiority of this approach compared to traditional numerical techniques. This exact solution describes a bright soliton steadily propagating on a periodic wave background. Mathematically, it is expressed as a linear superposition of a hyperbolic secant-squared (sech²) profile—representing the localized soliton—together with sinusoidal and cosine terms that constitute the periodic background, plus a constant offset. Physically, the solution captures a coherent structure that maintains its shape and amplitude while traveling through an oscillatory medium, illustrating the nonlinear balance between dispersion and periodic modulation, as observed in systems such as nonlinear optics, fluid dynamics, and plasma waves. To briefly analyze its dynamic characteristics, we now visualize the analytical solution obtained. The spatiotemporal dynamical visualization of the analytical solution of the (3+1)–dimensional Jimbo–Miwa equation is shown in Figure 3.

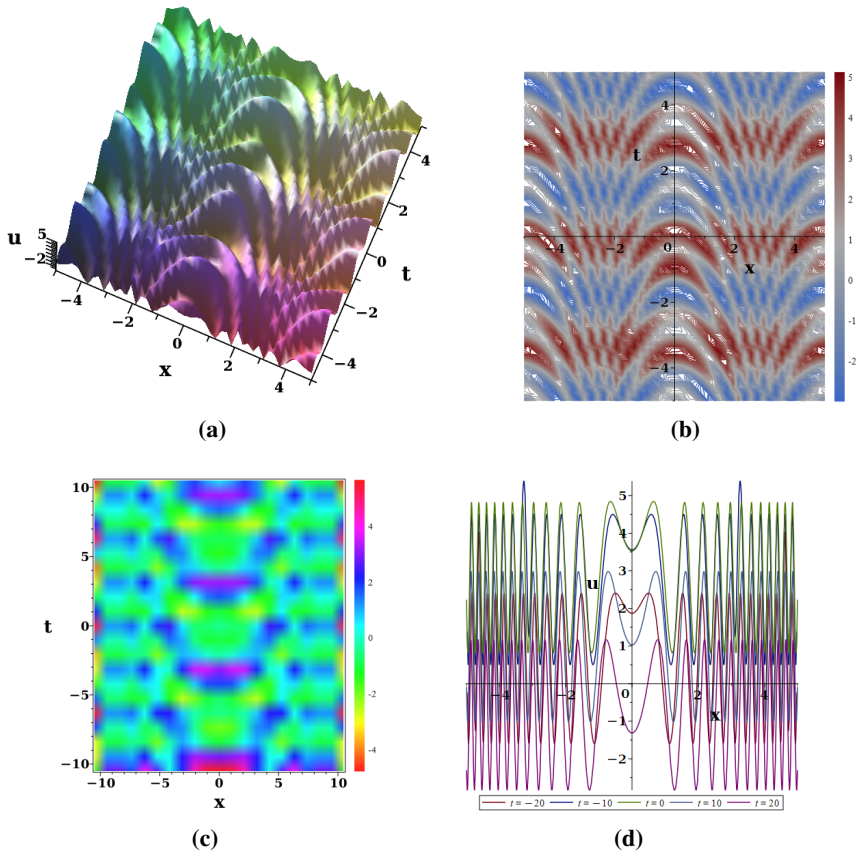

Figure 3. Plots of the solution equation (3.4) with $y = x^2, z = 1$: (**a**) Three-dimensional graphs; (**b**) contour diagrams; (**c**) thermal maps; (**d**) evolution plot.

Figure 3 presents a multi-faceted visualization of the exact solution given by Eq (3.4). The three-dimensional surface plot reveals the quasi-periodic oscillatory structure of the wave and its bidirectional propagation along the x-axis. Contour lines and a corresponding heatmap detail the localized energy distribution, showing high-amplitude wave packets superimposed on a periodic background—a hallmark of nonlinear localization. Cross-sectional profiles at different time instants further confirm the stable propagation and shape-preserving nature of the waveform. Collectively, these graphical representations illustrate the key dynamical features of the solution, including its spatiotemporal periodicity, strong localization induced by the sech^2 term, and the sustained wave structure resulting from the balance between dispersion and nonlinearity.

For Case 2, we substitute Eq (3.3) into (3.1). Simplifying the result yields the analytical solution for the (3+1)–dimensional Jimbo–Miwa equation, as shown in Eq (3.5).

$$\begin{aligned} u = b_4 &+ w_{1,u} \cdot \text{sech}^2\left(\frac{2yw_{y,1}^2 + ((3t+2z)w_{z,1} + 2b_2)\,w_{y,1} + 3tw_{z,1}^2}{2w_{y,1}}\right) \\ &+ w_{2,u} \cdot \sin\left(\frac{3tw_{z,2}(w_{y,2} + w_{z,2})}{2w_{y,2}} + yw_{y,2} + zw_{z,2} + b_3\right) \\ &+ w_{3,u} \cdot \cos\left(\frac{3tw_{z,3}(w_{y,3} + w_{z,3})}{2w_{y,3}} + yw_{y,3} + zw_{z,3} + b_5\right). \end{aligned} \tag{3.5}$$

Likewise, to assess the dependability of the result in Eq (3.5), we input the analytical solution of (3.5) into the left-hand side of the (3+1)–dimensional Jimbo–Miwa equation (1.1) and utilize Maple software to refine the outcome. The analysis confirms that the left-hand side of Eq (1.1) consistently equals zero, suggesting that the analytical solution (3.5) is dependable. This solution corresponds to a breather soliton on a periodic background. Mathematically, it takes the form of a linear superposition comprising a hyperbolic-secant-squared (bright soliton) term, sinusoidal and cosine terms representing the periodic carrier waves, and a constant offset. Dynamically, the soliton propagates steadily through the periodic background while its amplitude undergoes periodic oscillations—a characteristic breathing behavior. In contrast to the first solution (5), which describes a steady bright soliton with constant amplitude, the present solution incorporates pronounced spatiotemporal modulation that transforms the solitary wave into a dynamically breathing structure. The resulting spatiotemporal dynamical visualization of the analytical solution to the (3+1)–dimensional Jimbo–Miwa equation is shown in Figure 4.

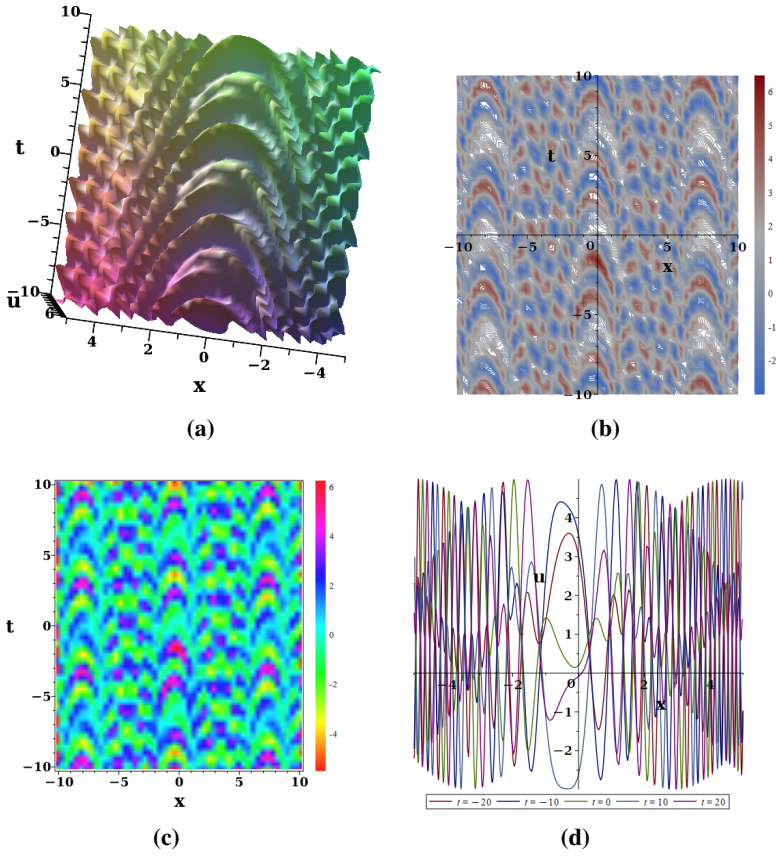

Figure 4. Plots of the solution equation (3.5) with $y = x^2, z = 1$: (**a**) Three-dimensional graphs; (**b**) contour diagrams; (**c**) thermal maps; (**d**) evolution plot.

Figure 4 visualizes the exact solution from Eq (3.5), a breather-soliton superposed on a periodic background. Panel (a) shows the solution's amplitude surface in the x–t plane. The surface displays helical folding, indicating strong nonlinear–dispersive coupling. Wave crests extend along a composite direction, corresponding to non-uniform propagation in the high-dimensional space. In panel (b), contours reveal fragmented, open regions of high amplitude. This pattern differs from

regular localized wave packets and suggests dynamic reorganization of the wave structure. The low-amplitude background shows disordered striations, reflecting enhanced multi-directional interference in the (3+1)D system. The corresponding heatmap in panel (c) highlights an asymmetric periodic arrangement of amplitude. This breaks the spatiotemporal symmetry seen in previous solutions, confirming a symmetry-broken state. Panel (d) plots cross-sectional profiles at $t = -20, -10, 0, 10, 20$. The wave propagates bidirectionally with strong amplitude modulation. The central peak is highest at $t = 0$, and the asymmetry between the wave flanks grows over time, underscoring nonlinear energy localization. Variations in oscillation frequency further indicate dynamic dispersion changes during propagation. Together, these panels characterize a dynamic, symmetry-broken waveform, illustrating the rich solution space of the (3+1)-dimensional Jimbo–Miwa equation.

3.2. Model [4-3-1]-2

To obtain different analytical solutions for neural network models with the same number of layers, we changed the activation functions in the hidden layers without changing the number of layers in the network model. We set the activation functions as $F_1(\xi_1) = \tanh^2(\xi_1)$, $F_2(\xi_2) = (\xi_2)^2$, $F_3(\xi_3) = (\xi_3)^2$, resulting in the model shown in Figure 2(c), [4-3-1]-2. By applying the output of the neural network model, we obtain the test function (3.6).

$$\begin{aligned} u^* = {} & b_4 + w_{1,u} \cdot \tanh^2\Big(tw_{t,1} + xw_{x,1} + yw_{y,1} + zw_{z,1} + b_2\Big) \\ & + w_{2,u} \cdot \Big(tw_{t,2} + xw_{x,2} + yw_{y,2} + zw_{z,2} + b_3\Big)^2 + w_{3,u} \cdot \Big(tw_{t,3} + xw_{x,3} + yw_{y,3} + zw_{z,3} + b_5\Big)^2. \end{aligned} \tag{3.6}$$

We differentiate the test function (3.6) and substitute it back into (1.1) to obtain a more complex equation. We collect the coefficients of each term to obtain the corresponding underdetermined nonlinear algebraic equation system. We then use Maple to solve this equation system and obtain two sets of coefficient solutions, Case 1 and Case 2, as shown in (3.7) and (3.8), respectively.

$$\textbf{Case 1:} \begin{cases} b_3 = b_3, & b_5 = b_5, \\ w_{1,u} = w_{1,u}, & w_{2,u} = w_{2,u}, \\ w_{3,u} = w_{3,u}, & \\ w_{t,1} = w_{t,1}, & w_{t,2} = w_{t,2}, \\ w_{t,3} = w_{t,3}, & \\ w_{x,1} = -w_{z,1}, & \\ w_{x,2} = -\frac{w_{2,u}w_{z,2}^2 + w_{3,u}w_{x,3}w_{z,3} + w_{3,u}w_{z,3}^2}{w_{2,u}w_{z,2}}, & \\ w_{x,3} = w_{x,3}, & \\ w_{y,1} = 0, & w_{y,2} = 0, \\ w_{y,3} = 0, & \\ w_{z,1} = w_{z,1}, & w_{z,2} = w_{z,2}, \\ w_{z,3} = w_{z,3}. & \end{cases} \tag{3.7}$$

$$\textbf{Case 2:}\quad \begin{cases} b_3 = b_3, & b_5 = b_5, & \\ w_{1,u} = w_{1,u}, & w_{2,u} = -\frac{w_{3,u}w_{x,3}^2}{w_{x,2}^2}, & w_{3,u} = w_{3,u}, \\ w_{t,1} = \frac{3w_{z,1}(w_{y,1}+w_{z,1})}{2w_{y,1}}, & w_{t,2} = w_{t,2}, & w_{t,3} = w_{t,3}, \\ w_{x,1} = 0, & w_{x,2} = w_{x,2}, & w_{x,3} = w_{x,3}, \\ w_{y,1} = w_{y,1}, & w_{y,2} = 0, & w_{y,3} = 0, \\ w_{z,1} = w_{z,1}, & w_{z,2} = \frac{w_{x,2}w_{z,3}}{w_{x,3}}, & w_{z,3} = w_{z,3}. \end{cases} \tag{3.8}$$

For Case 1, we substitute (3.7) into (3.6) and simplify to obtain the analytical solution of the (3+1)–dimensional Jimbo–Miwa equation as shown in (3.9).

$$u = b_4 + \frac{w_{2,u}}{w_{y,2}^2}\cdot\left(\frac{3tw_{z,2}^2}{2} + w_{y,2}\left(\frac{3t}{2}+z\right)w_{z,2} + w_{y,2}\left(yw_{y,2}+b_3\right)\right)^2. \tag{3.9}$$

To verify the accuracy of the results, the analytical solution (3.9) was substituted back into the left-hand side of the (3+1)–dimensional Jimbo–Miwa equation (1.1). Using Maple for symbolic computation, the expression was simplified to identically zero. This confirms that (3.9) is an exact solution, demonstrating its reliability and precision. The spatiotemporal evolution and dynamical characteristics of this analytical solution are visualized in Figures 5(a–d).

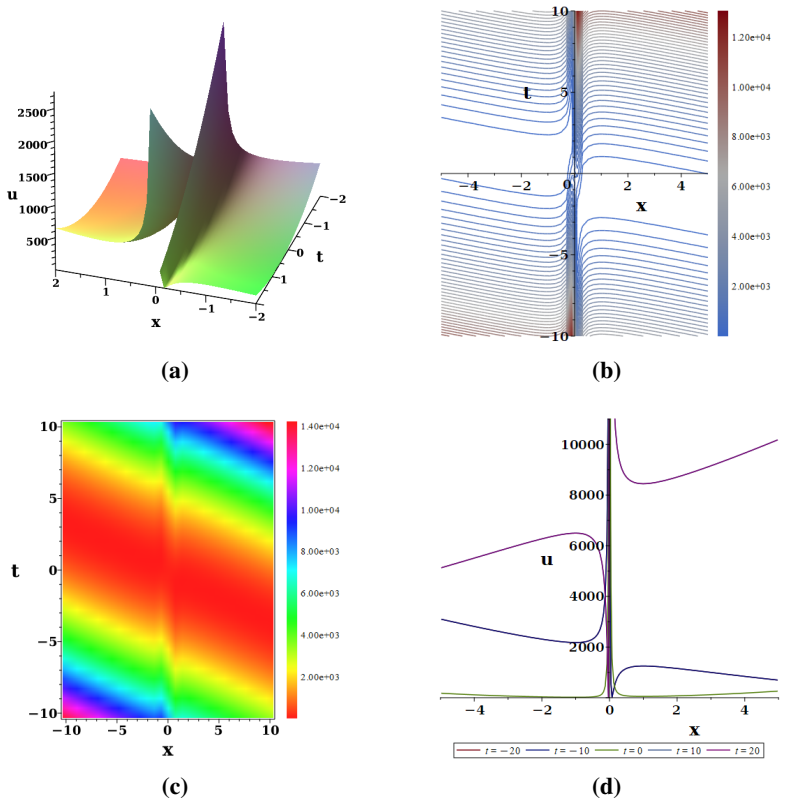

Figure 5. Plots of solution (3.9) with(3.9)with $y = x^2, z = x$: (**a**) Three-dimensional graphs; (**b**) contour diagrams; (**c**) thermal maps; (**d**) evolution plot.

Figure 5 visualizes the parabolic-type solution given by Eq (3.9). Figure 5(a) shows a sharp, ridge-like surface aligned with the t-axis, indicating strong line-localization of the wave energy near $x = 0$. The surface decays rapidly away from the ridge, highlighting the confinement of energy. In Figure 5(b), dense contours near $x = 0$ fan out along the t-axis, confirming the one-dimensional energy distribution. The corresponding heatmap in Figure 5(c) shows a bright strip along $x = 0$, with symmetric and steep decay on both sides, illustrating spatial inversion symmetry and dominant nonlinear self-focusing. Figure 5(d) plots the cross-sectional profiles at $t = -20, -10, 0, 10, 20$. A sharp peak remains fixed at $x = 0$ for all times, demonstrating clear spatiotemporal locking. The amplitude varies only slightly, and the waveform shape is preserved, confirming a stable, strongly localized structure that propagates within a low-dimensional subspace.

For Case 2, if we substitute (3.8) into (3.6) and simplify, we obtain another analytical solution for the (3+1)–dimensional Jimbo–Miwa equation, as shown in (3.10).

$$\begin{aligned} u = {} & b_4 + w_{1,u} \cdot \tanh^2\left(\frac{2yw_{y,1}^2 + ((3t+2z)w_{z,1} + 2b_2)\, w_{y,1} + 3tw_{z,1}^2}{2w_{y,1}}\right) \\ & - \frac{w_{3,u}}{w_{x,2}^2} \cdot \left(\left(tw_{t,2} + xw_{x,2} + b_3\right) w_{x,3} + zw_{x,2}w_{z,3}\right)^2 + w_{3,u} \cdot \left(tw_{t,3} + xw_{x,3} + zw_{z,3} + b_5\right)^2 . \end{aligned} \tag{3.10}$$

To confirm the validity of the analytical solution (3.10), it is substituted into the (3+1)–dimensional Jimbo–Miwa equation (1.1). The equation is satisfied identically, verifying that the solution is exact. Visualizing the obtained analytical solution, we take the corresponding parameters resulting in the analytical solution's spatiotemporal dynamics visualization diagram shown in Figure 6.

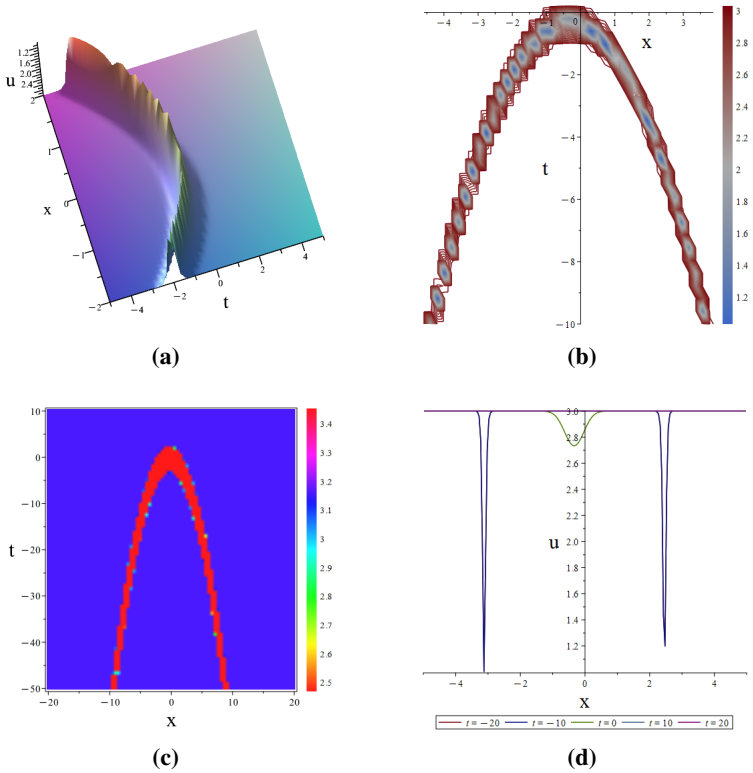

Figure 6. Plots of solution (3.10) with $y = x^2, z = x$: (**a**) Three-dimensional graphs; (**b**) contour diagrams; (**c**) thermal maps; (**d**) evolution plot.

From a top-down view, the three-dimensional surface in Figure 6(a) displays sawtooth-like wrinkles along the edges of the plateau, deviating from a perfectly flat top. This indicates that quasi-periodic amplitude modulation persists even within the highly localized region, reflecting the interplay between nonlinearity-driven energy confinement and dispersion-induced weak oscillations in high-dimensional systems. The red closed contours in Figure 6(b) outline arched localized regions, with jagged edges matching the surface wrinkles and confirming quasi-periodic modulation inside the localized area. The contours extend along the negative t-axis up to $t \approx -10$, suggesting a unidirectional propagation preference. In the heatmap of Figure 6(c), red arched bands follow an arched trajectory with rapid intensity decay away from the center. The vertices lie near $t \approx 0$ and $x \approx 0$. As t decreases, the bands spread symmetrically along the x-axis, highlighting the non-trivial arched propagation path in the negative t-direction. Figure 6(d) shows cross-sectional profiles at $t = -20, -10, 0, 10$, and 20. At $t = 0$, sharp minima appear at $x \approx \pm 2$ while the central amplitude remains high and stable. As $|t|$ increases, the valleys become shallower and the central amplitude decays slightly, revealing that strict localization occurs only near $t = 0$ and gradually weakens during propagation.

4. Double layer

4.1. Model [4-4-3-1]

To extract more solution sets from underdetermined systems of equations and reveal the rich dynamical properties of high-dimensional equations, we now increase the complexity of the model by constructing a neural network with two hidden layers to solve the (3+1)–dimensional Jimbo–Miwa equation as shown in Figure 7(a), which depicts the [4-4-3-1] two-layer hidden neural network model we have constructed. The input layer consists of four neurons, denoted as x, y, z, and t. The first hidden layer contains four neurons, denoted as $F_1(\xi_1)$, $F_2(\xi_2)$, $F_3(\xi_3)$ and $F_4(\xi_4)$, the second hidden layer contains three neurons, represented as $F_5(\xi_5)$, $F_6(\xi_6)$, and $F_7(\xi_7)$, and the final output layer is the output probe function $f(x, y, z, t)$. Now, we construct the activation function based on Figure 7(a), $F_1(\xi_1) = \cos(\xi_1)$, $F_2(\xi_2) = \sin(\xi_2)$, $F_3(\xi_3) = \tanh(\xi_3)$, $F_4(\xi_4) = sech(\xi_4)$, $F_5(\xi_5) = (\xi_5)^2$, $F_6(\xi_6) = (\xi_6)^2$, $F_5(\xi_7) = (\xi_7)^2$, resulting in the model shown in Figure 7(b), [4-3-1]-1. By applying the output of the neural network model, we obtain the probe function (4.1).

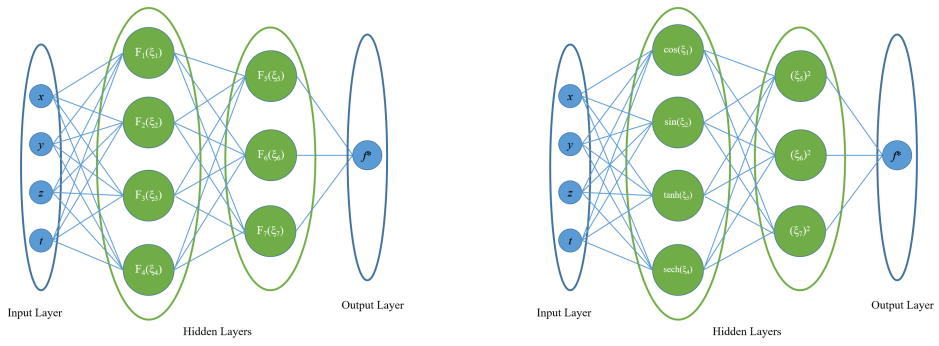

(a) **(b)**

Figure 7. Double-hidden-layer neural network model diagram: (**a**) Network structure; (**b**) Model [4-4-3-1]-1.

$$
\begin{aligned}
u^* = b_8 &+ w_{5,u}\Big(w_{1,5}\cos\Big(tw_{t,1} + xw_{x,1} + yw_{y,1} + zw_{z,1} + b_1\Big) \\
&+ w_{2,5}\sin\Big(tw_{t,2} + xw_{x,2} + yw_{y,2} + zw_{z,2} + b_2\Big) \\
&+ w_{3,5}\tanh\Big(tw_{t,3} + xw_{x,3} + yw_{y,3} + zw_{z,3} + b_3\Big) \\
&+ w_{4,5}\,\mathrm{sech}\Big(tw_{t,4} + xw_{x,4} + yw_{y,4} + zw_{z,4} + b_4\Big) \\
&+ b_5\Big)^2 \\
&+ w_{6,u}\Big(w_{1,6}\cos\Big(tw_{t,1} + xw_{x,1} + yw_{y,1} + zw_{z,1} + b_1\Big) \\
&+ w_{2,6}\sin\Big(tw_{t,2} + xw_{x,2} + yw_{y,2} + zw_{z,2} + b_2\Big) \\
&+ w_{3,6}\tanh\Big(tw_{t,3} + xw_{x,3} + yw_{y,3} + zw_{z,3} + b_3\Big) \\
&+ w_{4,6}\,\mathrm{sech}\Big(tw_{t,4} + xw_{x,4} + yw_{y,4} + zw_{z,4} + b_4\Big) \\
&+ b_6\Big)^2 \\
&+ w_{7,u}\Big(w_{1,7}\cos\Big(tw_{t,1} + xw_{x,1} + yw_{y,1} + zw_{z,1} + b_1\Big) \\
&+ w_{2,7}\sin\Big(tw_{t,2} + xw_{x,2} + yw_{y,2} + zw_{z,2} + b_2\Big) \\
&+ w_{3,7}\tanh\Big(tw_{t,3} + xw_{x,3} + yw_{y,3} + zw_{z,3} + b_3\Big) \\
&+ w_{4,7}\,\mathrm{sech}\Big(tw_{t,4} + xw_{x,4} + yw_{y,4} + zw_{z,4} + b_4\Big) \\
&+ b_7\Big)^2 .
\end{aligned} \tag{4.1}
$$

Following the single-hidden-layer approach, the expressions are differentiated and substituted into Eq (4.1). Applying the NNSCA method yields two coefficient solutions: Case 1 (4.2) and Case 2 (4.3).

$$
\textbf{Case 1:}\quad \begin{cases}
b_5 = b_5, & b_6 = b_6, & b_7 = b_7, & \\
w_{1,5} = w_{1,5}, & w_{1,6} = w_{1,6}, & & \\
w_{2,5} = w_{2,5}, & w_{2,6} = w_{2,6}, & & \\
w_{3,5} = w_{3,5}, & w_{3,6} = w_{3,6}, & & \\
w_{4,5} = w_{4,5}, & w_{4,6} = w_{4,6}, & & \\
w_{t,1} = 0, & w_{t,2} = 0, & w_{t,3} = 0, & \\
w_{t,4} = \frac{3w_{z,4}(w_{y,4}+w_{z,4})}{2w_{y,4}}, & & & \\
w_{x,1} = 0, & w_{x,2} = 0, & w_{x,3} = 0, & w_{x,4} = 0, \\
w_{y,1} = 0, & w_{y,2} = 0, & w_{y,3} = 0, & w_{y,4} = w_{y,4}, \\
w_{z,1} = 0, & w_{z,2} = 0, & w_{z,3} = 0, & w_{z,4} = w_{z,4}, \\
w_{5,u} = w_{5,u}, & w_{6,u} = w_{6,u}, & w_{7,u} = w_{7,u}. &
\end{cases} \tag{4.2}
$$

$$\textbf{Case 2:}\quad \begin{cases} b_5 = b_5, & b_6 = b_6, & b_7 = b_7, & \\ w_{1,5} = w_{1,5}, & w_{1,6} = 0, & & \\ w_{2,5} = w_{2,5}, & w_{2,6} = w_{2,6}, & & \\ w_{3,5} = w_{3,5}, & w_{3,6} = 0, & & \\ w_{4,5} = 0, & w_{4,6} = w_{4,6}, & & \\ w_{t,1} = 0, & w_{t,2} = 0, & & \\ w_{t,3} = \frac{3w_{z,3}(w_{y,3}+w_{z,3})}{2w_{y,3}}, & w_{t,4} = w_{t,4}, & & \\ w_{x,1} = 0, & w_{x,2} = 0, & w_{x,3} = 0, & w_{x,4} = 0, \\ w_{y,1} = 0, & w_{y,2} = 0, & w_{y,3} = w_{y,3}, & w_{y,4} = 0, \\ w_{z,1} = 0, & w_{z,2} = 0, & w_{z,3} = w_{z,3}, & w_{z,4} = 0, \\ w_{5,u} = w_{5,u}, & w_{6,u} = w_{6,u}, & w_{7,u} = w_{7,u}. & \end{cases} \tag{4.3}$$

For Case 1 (4.2), substituting the coefficients into Eq (4.1) and simplifying directly yields the analytical solution of the (3+1)–dimensional Jimbo–Miwa equation (Eq (4.4)).

$$\begin{aligned} u = b_8 &+ w_{5,u} \cdot \Bigg(w_{1,5}\cos(b_1) + w_{2,5}\sin(b_2) + w_{3,5}\tanh(b_3) \\ &\quad + w_{4,5}\,sech\left(\frac{2w_{y,4}^2 y + \left((3t+2z)w_{z,4} + 2b_4\right)w_{y,4} + 3tw_{z,4}^2}{2w_{y,4}}\right) + b_5 \Bigg)^2 \\ &+ w_{6,u} \cdot \Bigg(w_{1,6}\cos(b_1) + w_{2,6}\sin(b_2) + w_{3,6}\tanh(b_3) \\ &\quad + w_{4,6}\,sech\left(\frac{2w_{y,4}^2 y + \left((3t+2z)w_{z,4} + 2b_4\right)w_{y,4} + 3tw_{z,4}^2}{2w_{y,4}}\right) + b_6 \Bigg)^2 \\ &+ w_{7,u} \cdot \Bigg(w_{1,7}\cos(b_1) + w_{2,7}\sin(b_2) + w_{3,7}\tanh(b_3) \\ &\quad + w_{4,7}\,sech\left(\frac{2w_{y,4}^2 y + \left((3t+2z)w_{z,4} + 2b_4\right)w_{y,4} + 3tw_{z,4}^2}{2w_{y,4}}\right) + b_7 \Bigg)^2. \end{aligned} \tag{4.4}$$

This solution describes a peaked traveling wave formed by multi-mode coupling. It is constructed by squaring and summing three function terms of similar form but with distinct weights. Each term combines trigonometric functions (cos, sin, tanh) with a propagating hyperbolic-secant soliton profile, and the expression contains multiple free parameters. We visualize the analytical solution obtained by setting the corresponding parameters, resulting in the analytical solution's spatiotemporal dynamics visualization diagram shown in Figure 8.

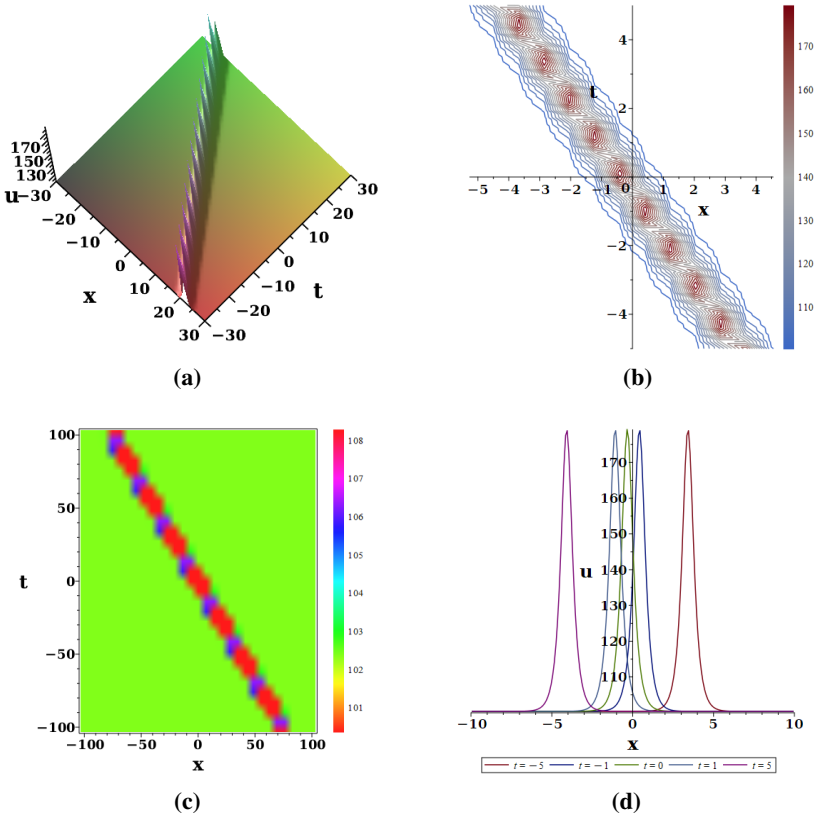

Figure 8. Plots of solution (4.4) with $y = x, z = x$: (**a**) Three-dimensional graphs; (**b**) contour diagrams; (**c**) thermal maps; (**d**) evolution plot.

The graph in Figure 8(a) confirms the wave's strong preference for directional propagation. The dual-hidden-layer model captures this regular trajectory with high precision. Deeper feature abstraction reveals the underlying diagonal conservation law of the (3+1)–dimensional Jimbo–Miwa solution. In the contour diagram (Figure 8(b)), red closed vortices arrange periodically along the diagonal. Each vortex shows an amplitude difference exceeding 30 between the center and edge. This highlights strong energy concentration in localized pulses. The wavy extension of blue outer lines resonates with the vortex period. It suggests a cyclic mechanism of pulse generation and annihilation. The pseudo-color thermal map (Figure 8(c)) displays red high-amplitude spots distributed at equal intervals along the diagonal. Strong contrast with the green background emphasizes the periodicity and isolation of the pulse trains. The narrow color scale indicates stable energy levels. Through complex feature transformations, the double-hidden-layer model reveals the periodic pulse flow pattern. This offers a fresh perspective on dynamic transport in high-dimensional systems. The evolution plots (Figure 8(d)) show x-profile curves at $t = -5, -1, 0, 1, 5$. Sharp peaks move linearly along the x-axis with time. Propagation occurs strictly along the $x + t$ direction. Peak amplitudes remain stable. Half-widths stay narrow. These features indicate motion-invariant solitons. The dual-hidden-layer architecture successfully extracts this directional periodic soliton solution from an underdetermined equation system. It demonstrates the model's ability to reveal intricate dynamics in high-dimensional integrable equations.

For Case 2, we substitute Eq (4.3) into Eq (4.1) and simplify. This yields another analytical solution

of the (3+1)–dimensional Jimbo–Miwa equation, given by Eq (4.5).

$$u = b_8 + w_{5,u} \cdot \left(w_{1,5} \cos(b_1) + w_{2,5} \sin(b_2) \right. \tag{4.5}$$
$$\left. + w_{3,5} \tanh\left(\frac{2w_{y,3}^2 y + ((3t + 2z)w_{z,3} + 2b_3)\, w_{y,3} + 3w_{z,3}^2 t}{2w_{y,3}} \right) + b_5 \right)^2$$
$$+ w_{6,u} \cdot \left(w_{2,6} \sin(b_2) + w_{4,6} sech(t w_{t,4} + b_4) + b_6 \right)^2 + w_{7,u} \cdot \left(w_{2,7} \sin(b_2) + w_{4,7} sech(t w_{t,4} + b_4) + b_7 \right)^2.$$

For Case 2, we substitute Eq (4.3) into Eq (4.1) and simplify. This yields another analytical solution of the (3+1)–dimensional Jimbo–Miwa equation, given by Eq (4.5). This solution constitutes a composite wave pattern that combines multiple solitons and kink-type structures. Mathematically, it is expressed as a weighted sum of three squared terms, each coupling trigonometric and hyperbolic functions, representing an exact superposition of distinct nonlinear modes. Dynamically, the solution describes several well-localized wave peaks that propagate independently while preserving their multi-peaked shape without dispersion—a hallmark of integrable systems in which coherent structures can coexist and evolve in parallel without interaction. Visualizing the obtained analytical solution, we take the corresponding parameters, resulting in the spatiotemporal dynamical visualization diagrams of the analytical solutions shown in Figure 9.

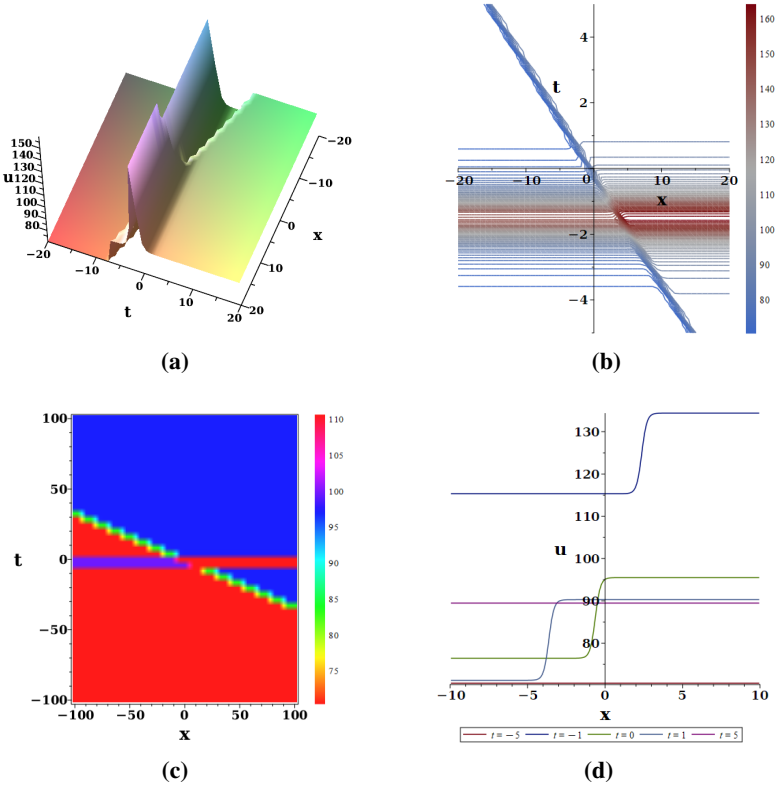

Figure 9. Plots of solution (4.5) with $y = x, z = x$: (**a**) Three-dimensional graphs; (**b**) contour diagrams; (**c**) thermal maps; (**d**) evolution plot.

Figure 9 illustrates the spatiotemporal bifurcation structure of solutions to the (3+1)–dimensional Jimbo–Miwa equation, captured through a dual-hidden-layer model. In the three-dimensional graph (Figure 9(a)), the surface exhibits a sharp bifurcation near $x \approx 0$ and $t \approx 0$. The amplitude jumps abruptly from a low-energy state on the left to a high-energy state on the right. This forms a steep interface. The model's dual hidden layers enable it to represent nonlinear bifurcation behavior. Solutions undergo essential transformations under specific spatiotemporal thresholds. This reflects phase transition-like evolution in nonlinear systems. The contour diagrams (Figure 9(b)) show blue lines intersecting red high-amplitude regions at the bifurcation interface. Complex interference patterns emerge. High-amplitude regions remain confined near the interface. This indicates energy localization. Nonlinear waves propagate along the boundary, similar to waveguides in high-dimensional systems. The dual hidden layers abstract deep features. They overcome limitations of simpler models in characterizing linear interfaces. Thermal maps (Figure 9(c)) display stable red and blue blocks in upper and lower regions. A diagonal transition zone marks the critical area for state changes. This reveals bistable and multistable characteristics. The system maintains two energy states. Transitions occur only in critical spacetime regions. The dual layers' expressive power extracts threshold-driven transitions from underdetermined equations. It highlights complex dynamics in high-dimensional systems. Evolution plots (Figure 9(d)) examine x cross-sections at $t = -5, -1, 0, 1,$ and 5. At $t = -5$, amplitude stays extremely low. At $t = -1$, it jumps rapidly near $x \approx 0$. For $t \geq 0$, it stabilizes in a high-energy state. This confirms a threshold excitation mechanism. Nonlinear effects trigger and sustain wave excitation beyond critical values. The dual hidden layers facilitate analysis of this trigger-to-sustain dynamics.

5. Conclusions

This study presents the NNSCA, a novel framework that merges symbolic computation with neural networks. The NNSCA derives exact analytical solutions for high-dimensional nonlinear PDEs without requiring specialized equation transformations, such as a conversion to bilinear form. We demonstrate the method on the (3+1)–dimensional Jimbo–Miwa equation using both single-hidden-layer and double-hidden-layer network architectures. These models enforce exact differential constraints symbolically, eliminating the need to presuppose a solution's functional form. Using the NNSCA, we obtained multiple classes of exact solutions, including solitons, breathers, shock waves, and lumps. Single-hidden-layer networks captured fundamental wave structures, while a double-hidden-layer architecture revealed more complex, spatiotemporally coupled dynamics—highlighting the importance of network depth. The solutions correspond to physical wave phenomena in fluids, optics, and plasmas. Detailed visualizations illustrate their four-dimensional evolution, showcasing wave interference, propagation, and modulation, and thereby confirming their physical consistency.

Compared to traditional numerical schemes and the Hirota bilinear method, the NNSCA offers greater automation, broader applicability, and access to a wider variety of solution types. The successful application of the NNSCA underscores the potential of tightly integrating symbolic and neural frameworks. It opens a systematic, algebraically grounded pathway for analyzing the rich solution landscape of high-dimensional nonlinear systems. Several challenges remain, such as scaling the method to larger parameter systems and avoiding trivial parameter reductions during constraint

solving. Addressing these will be the focus of future work.

Author contributions

Yu Gao: Conceptualization, Resources, Software, Funding acquisition, Writing-review & editing, Visualization, Project administration; Jingwen Huang: Writing-original draft, Software, Visualization; Baoying Du: Resource, Writing-original draft, Methodology, Visualization; Jianglong Shen: Conceptualization, Resources, Software, Methodology. All authors contributed equally to the preparation of this manuscript. All authors have read and approved the final version of the manuscript for publication.

Use of Generative-AI tools declaration

The authors declare that they have not used Artificial Intelligence (AI) tools in the creation of this article.

Funding

This research was supported by the High-Level Talent Sailing Project of Yibin University (No. 2021QH07).

Conflict of interest

The authors declare that they have no conflict of interest concerning the publication of this manuscript.

References

1. C. Wang, J. Qi, Q. Zhang, Global well-posedness for the 2D Keller-Segel-Navier-Stokes system with fractional diffusion, *Acta Appl. Math.*, **194** (2024), 7–12. https://doi.org/10.1007/s10440-024-00696-5
2. G. Yel, H. M. Baskonus, H. Bulut, Novel archetypes of new coupled Konno–Oono equation by using sine–Gordon expansion method, *Opt. Quantum Elect.*, **49** (2017), 285–293. https://doi.org/10.1007/s11082-017-1127-z
3. R. Rrey, U. Polte, Nonlinear Black–Scholes equations in finance: Associated control problems and properties of solutions, *SIAM J. Control Optim.*, **49** (2011), 185–204. https://doi.org/10.1137/090773647
4. J. Xu, S. Xie, H. Fu, Maximum-norm error estimates of fourth-order compact and ADI compact finite difference methods for nonlinear coupled bacterial systems, *J. Sci. Comput.*, **100** (2024), 33–40. https://doi.org/10.1007/s10915-024-02588-0
5. A. H. Arnous, M. Mirzazadeh, A. Akbulut, L. Akinyemi, Optical solutions and conservation laws of the Chen-Lee-Liu equation with Kudryashov's refractive index

via two integrable techniques, *Waves Random Complex Media*, **35** (2022), 2607–2623. https://doi.org/10.1080/17455030.2022.2045044

6. R. M. El-Shiekh, M. Gaballah, Solitary chirp pulses and soliton control for variable coefficients cubic–quintic nonlinear Schrödinger equation in nonuniform management system, *Open Phys.*, **23** (2025), 20250147. https://doi.org/10.1515/phys-2025-0147
7. Y. Song, B. Yang, Z. Wang, Bifurcations and exact solutions of a new (3+1)-dimensional Kadomtsev-Petviashvili equation, *Phys. Lett. A*, **461** (2023), 128647. https://doi.org/10.1016/j.physleta.2023.128647
8. D. Lin, X. Yuan, X. Su, Local entropy generation in compressible flow through a high pressure turbine with delayed detached eddy simulation, *Entropy*, **19** (2017), 29–34. https://doi.org/10.3390/e19010029
9. A. Melet, P. Teatini, G. Le Cozannet, C. Jamet, A. Conversi, J. Benveniste, et al., Earth observations for monitoring marine coastal hazards and their drivers, *Surveys Geophys.*, **41** (2020), 1489–1534. https://doi.org/10.1007/s10712-020-09594-5
10. M. Jimbo, T. Miwa, Solitons and infinite dimensional Lie algebras, *Publ. Res. Inst. Math. Sci.*, **19** (1983), 943–1001. https://doi.org/10.2977/prims/1195182017
11. P. Xu, B. Q. Zhang, H. Huang, K. J. Wang, Study on the nonlinear dynamics of the (3+1)-dimensional Jimbo–Miwa equation in plasma physics, *Axioms*, **12** (2023), 592–598. https://doi.org/10.3390/axioms12060592
12. X. W. Yan, S. F. Tian, M. J. Dong, T. T. Zhang, Dynamics of lump solutions, lump-kink solutions and periodic lump solutions in a (3+1)-dimensional generalized Jimbo–Miwa equation, *Waves Random Complex Media*, **31** (2019), 293–304. https://doi.org/10.1080/17455030.2019.1582823
13. S. K. Dhiman, S. Kumar, H. Kharbanda, An extended (3+1)-dimensional Jimbo–Miwa equation: Symmetry reductions, invariant solutions and dynamics of different solitary waves, *Modern Phys. Lett. B*, **35** (2021), 2150528. https://doi.org/10.1142/S0217984921505254
14. Y. Liu, J. Manafian, N. A. Alkader, B. Eslami, On soliton solutions, periodic wave solutions, asymptotic analysis and interaction phenomena of the (3+1)-dimensional JM equation, *Modern Phys. Lett. A*, **38** (2023), 2350118. https://doi.org/10.1142/S0217732323501183
15. A. R. Seadawy, H. Zahed, M. Iqbal, Solitary wave solutions for the higher dimensional Jimo–Miwa dynamical equation via new mathematical techniques, *Mathematics*, **10** (2022), 1011. https://doi.org/10.3390/math10071011
16. H. D. Guo, T. C. Xia, B. B. Hu, High-order breathers and hybrid solutions for an extended (3 + 1)-dimensional Jimbo–Miwa equation in fluid dynamics, *Nonlinear Dyn.*, **100** (2020), 601–614. https://doi.org/10.1007/s11071-020-05514-9
17. Y. Zhang, S. Sun, H. Dong, Hybrid solutions of (3 + 1)-dimensional Jimbo–Miwa equation, *Math. Prob. Eng.*, **2017** (2017), 5453941. https://doi.org/10.1155/2017/5453941
18. J. Liu, X. Yang, M. Cheng, Y. Feng, Y. Wang, Abound rogue wave type solutions to the extended (3+1)-dimensional Jimbo–Miwa equation, *Comput. Math. Appl.*, **78** (2019), 1947–1959. https://doi.org/10.1016/j.camwa.2019.03.034

19. S. Srivastava, M. Kumar, Nonclassical symmetries, optimal classification, and dynamical behavior of similarity solutions of (3+1)-dimensional Burgers equation, *Chinese J. Phys.*, **89** (2024), 404–416. https://doi.org/10.1016/j.cjph.2024.03.019

20. X. W. Yan, S. F. Tian, X. B. Wang, T. T. Zhang, Solitons to rogue waves transition, lump solutions and interaction solutions for the (3+1)-dimensional generalized B-type Kadomtsev–Petviashvili equation in fluid dynamics, *Int. J. Comput. Math.*, **96** (2018), 1839–1848. https://doi.org/10.1080/00207160.2018.1535708

21. Y. Tang, Z. Liang, J. Ma, Exact solutions of the (3+1)-dimensional Jimbo–Miwa equation via Wronskian solutions: Soliton, breather, and multiple lump solutions, *Phys. Scr.*, **96** (2021), 095210. https://doi.org/10.1088/1402-4896/ac046a

22. P. P. Su, Y. N. Tang, Y. N. Chen, Wronskian and Grammian solutions for the (3+1)-dimensional Jimbo–Miwa equation, *Chinese Phys. B*, **21** (2012), 120509. https://doi.org/10.1088/1674-1056/21/12/120509

23. M. Song, Y. Ge, Application of the (G'/G)-expansion method to (3+1)-dimensional nonlinear evolution equations, *Comput. Math. Appl.*, **60** (2010), 1220–1227. https://doi.org/10.1016/j.camwa.2010.05.045

24. S. Sirisubtawee, S. Koonprasert, C. Khaopant, W. Porka, Two reliable methods for solving the (3 + 1)-dimensional space-time fractional Jimbo–Miwa equation, *Math. Prob. Eng.*, **2017** (2017), 9257019. https://doi.org/10.1155/2017/9257019

25. J. G. Liu, X. J. Yang, Y. Y. Feng, On integrability of the extended (3+1)-dimensional Jimbo–Miwa equation, *Math. Meth. Appl. Sci.*, **43** (2019), 1646–1659. https://doi.org/10.1002/mma.5991

26. M. Singh, New exact solutions for (3+1)-dimensional Jimbo–Miwa equation, *Nonlinear Dyn.*, **84** (2015), 875–880. https://doi.org/10.1007/s11071-015-2533-z

27. Z. Yan, New families of nontravelling wave solutions to a new (3+1)-dimensional potential-YTSF equation, *Phys. Lett. A*, **318** (2003), 78–83. https://doi.org/10.1016/j.physleta.2003.08.073

28. J. L. Shen, M. Liu, J. B. Liang, R. F. Zhang, New solutions to the (3+1)-dimensional HB equation using bilinear neural networks method and symbolic ansatz method using neural network architecture, *AIMS Math.*, **10** (2025), 30307–30330. https://doi.org/10.3934/math.20251331

29. X. Yong, X. Li, Y. Huang, General lump-type solutions of the (3+1)-dimensional Jimbo-Miwa equation, *Appl. Math. Lett.*, **86** (2018), 222–228. https://doi.org/10.1016/j.aml.2018.07.001

30. M. Gao, S. Zhou, W. Gu, Z. Wu, H. Liu, A. Zhou, et al., MMGPT4LF: Leveraging an optimized pre-trained GPT-2 model with multi-modal cross-attention for load forecasting, *Appl. Energy*, **392** (2025), 125965. https://doi.org/10.1016/j.apenergy.2025.125965

31. J. Yan, B. Hu, Z. H. Guan, D. X. Zhang, On controllability of fractional-order impulsive and switching systems with time delay, *Appl. Math. Comput.*, **497** (2025), 129357. https://doi.org/10.1016/j.amc.2025.129357

32. J. Wang, X. Feng, Y. Yu, X. Wang, N. Werghi, X. Han, et al., Fuzzy actor–critic learning-based interpretable control and stability-informed guarantee with error mapping for discrete-time nonlinear system, *Chaos Solitons Fract.*, **199** (2025), 116878. https://doi.org/10.1016/j.chaos.2025.116878

33. Y. Luo, J. Xu, Y. Chen, Y. Yang, T. Zheng, H. Liu, Optimal Hovering Control Strategy for UAVs Using PPO, In: *2025 7th International Conference on Machine Learning, Big Data and Business Intelligence*, **1133** (2025), 247–251. https://doi.org/10.1109/MLBDBI67855.2025.11331433
34. Z. Ma, A. Sun, Z. Zhang, Y. Yang, Z. Gao, H. Liu, Energy-constrained motion planning and scheduling for autonomous robots in complex environments, In: *2025 5th International Conference on Advanced Algorithms and Neural Networks (AANN)*, **13** (2025), 591–594. https://doi.org/10.1109/AANN66429.2025.11257590
35. Q. He, A unified metric architecture for AI infrastructure: A Cross-Layer taxonomy integrating performance, efficiency, and cost, preprint paper, 2025. https://doi.org/10.48550/arXiv.2511.21772
36. Q. He, C. Qu, Waste-to-energy-coupled AI data centers: Cooling efficiency and grid resilience, preprint paper, 2025. https://doi.org/10.48550/arXiv.2512.24683
37. Q. He, Location-Robust Cost-Preserving blended pricing for multi-Campus AI data centers, preprint paper, 2025. https://doi.org/10.48550/arXiv.2512.14197
38. Y. Hou, Y. Wang, X. Xia, Y. Tian, Z. Li, T. Q. S. Quek, Toward secure SAR image generation via federated Angle-Aware generative diffusion framework, *IEEE Internet Things J.*, **13** (2026), 2713–2730. https://doi.org/10.1109/JIOT.2025.3630329
39. Y. Hou, S. Zhao, X. Xia, M. Liwang, Z. Li, N. Xu, et al., FedC-DAC: A federated clustering with dynamic aggregation and calibration method for SAR image target recognition, *IEEE J. Selected Topics Appl. Earth Observ. Remote Sens.*, **19** (2026), 3726–3745. https://doi.org/10.1109/JSTARS.2025.3649421
40. K. Zhang, W. Luo, Y. Zhong, L. Ma, W. Liu, H. Li, Adversarial Spatio-Temporal learning for video deblurring, *IEEE Trans. Image Proc.*, **28** (2019), 291–301. https://doi.org/10.1109/TIP.2018.2867733
41. N. Chen, B. Li, Y. Wang, X. Ying, L. Wang, C. Zhang, et al., Motion and appearance decoupling representation for event cameras, *IEEE Trans. Image Proc.*, **34** (2025), 5964–5977. https://doi.org/10.1109/TIP.2025.3607632
42. J. Zhang, Y. Zhang, E. Yao, A new framework for traffic conflict identification by incorporating Ppredicted high-resolution trajectory and vehicle profiles in a CAV context, *Transport. Res. Record*, **2679** (2025), 445–462. https://doi.org/10.1177/03611981251348444
43. C. Lv, X. L. Lv, Z. Wang, T. Zhao, W. Tian, Q. Zhou, et al., A focal quotient gradient system method for deep neural network training, *Appl. Soft Comput.*, **184** (2025), 113704. https://doi.org/10.1016/j.asoc.2025.113704
44. G. Cybenko, Approximation by superpositions of a sigmoidal function, *Math. Control, Sign. Syst.*, **2** (1989), 303–314. https://doi.org/10.1007/BF02551274
45. M. Raissi, P. Perdikaris, G. E. Karniadakis, Physics-informed neural networks: A deep learning framework for solving forward and inverse problems involving nonlinear partial differential equations, *J. Comput. Phys.*, **378** (2019), 686–707. https://doi.org/10.1016/j.jcp.2018.10.045
46. R. F. Zhang, S. Bilige, Bilinear neural network method to obtain the exact analytical solutions of nonlinear partial differential equations and its application to p-gBKP equation, *Nonlinear Dyn.*, **95** (2019), 3041–3048. https://doi.org/10.1007/s11071-018-04739-z

47. J. B. Liang, B. Y. Du, X. Li, J. L. Shen, A new neural network framework integrating symbolic computation to solve the (2+1)-dimensional boussinesq equation, *Mathematics*, **14** (2026), 648. https://doi.org/10.3390/math14040648

48. X. Li, J. Shen, J. Liang, Y. Gao, Bilinear feature-enhanced symbolic computation neural network method for solving the (1+1)-dimensional Caudrey–Dodd–Gibbon equation, *AIMS Math.*, **11** (2026), 3193–3218. https://doi.org/10.3934/math.2026128

49. A. Mateen, G. H. Tipu, Z. Zhou, F. Javed, Nonlinear wave interactions and stability analysis in the CBS–nCBS model via bilinear neural network approach, *Modern Phys. Lett. B*, **40** (2026), 2650087. https://doi.org/10.1142/S0217984926500879

50. S. Akram, M. Rahman, L. A. AL-Essa, Inelastic lump–breather interactions and periodic wave dynamics in the generalized Calogero–Bogoyavlenskii–Schiff equation via a bilinear neural architecture, *Europ. Phys. J. Spec. Topics*, (2026), 1–20. https://doi.org/10.1140/epjs/s11734-026-02233-x

51. G. Zhu, H. Wang, Z. A. Mou, Y. Lin, Various solutions of the (2+1)-dimensional Hirota–Satsuma–Ito equation using the bilinear neural network method, *Chinese J. Phys.*, **83** (2023), 292–305. https://doi.org/10.1016/j.cjph.2023.03.016

52. R. F. Zhang, M. C. Li, J. Y. Gan, Q. Li, Z. Z. Lan, Novel trial functions and rogue waves of generalized breaking soliton equation via bilinear neural network method, *Chaos Solitons Fract.*, **154** (2022), 111692. https://doi.org/10.1016/j.chaos.2021.111692

53. J. L. Shen, X. Y. Wu, Periodic-soliton and periodic-type solutions of the (3+1)-dimensional Boiti–Leon–Manna–Pempinelli equation by using BNNM, *Nonlinear Dyn.*, **106** (2021), 831–840. https://doi.org/10.1007/s11071-021-06848-8

54. R. Lei, L. Tian, Z. Ma, Lump waves, bright-dark solitons and some novel interaction solutions in (3+1)-dimensional shallow water wave equation, *Phys. Scr.*, **99** (2024), 015255. https://doi.org/10.1088/1402-4896/ad16b6

55. C. Huang, Y. Zhu, K. Li, J. Li, R. Zhang, M-lump solutions, lump-breather solutions, and N-soliton wave solutions for the KP-BBM equation via the improved bilinear neural network method, *Nonlinear Dyn.*, **112** (2024), 21355–21368. https://doi.org/10.1007/s11071-024-10122-y

AIMS Press